

**Anatomy of ultrafast quantitative magnetoacoustics in freestanding nickel thin films**

Antonia Ghita <sup>1</sup>, Tudor-Gabriel Mocioi <sup>1</sup>, Alexey M. Lomonosov <sup>2</sup>, Jiwan Kim,<sup>3</sup> Oleksandr Kovalenko <sup>1</sup>,  
Paolo Vavassori <sup>4,5</sup> and Vasily V. Temnov <sup>1,\*</sup>

<sup>1</sup>*LSI, Ecole Polytechnique, CEA/DRF/IRAMIS, CNRS, Institut Polytechnique de Paris, F-91128 Palaiseau, France*

<sup>2</sup>*B+W Department, Offenburg University of Applied Sciences, 77652 Offenburg, Germany*

<sup>3</sup>*Department of Physics, Kunsan National University, 54150 Kunsan, Korea*

<sup>4</sup>*CIC nanoGUNE BRTA, E-20018 Donostia-San Sebastian, Spain*

<sup>5</sup>*IKERBASQUE, Basque Foundation for Science, E-48013 Bilbao, Spain*

 (Received 23 December 2022; revised 15 March 2023; accepted 31 March 2023; published 13 April 2023)

We revisit the quantitative analysis of the ultrafast magnetoacoustic experiment in a freestanding nickel thin film by Kim and Bigot [J.-W. Kim and J.-Y. Bigot, *Phys. Rev. B* **95**, 144422 (2017)] by applying our recently proposed approach of magnetic and acoustic eigenmode decomposition. We show that the application of our modeling to the analysis of time-resolved reflectivity measurements allows for the determination of amplitudes and lifetimes of standing perpendicular acoustic phonon resonances with unprecedented accuracy. The acoustic damping is found to scale as  $\propto \omega^2$  for frequencies up to 80 GHz, and the peak amplitudes reach  $10^{-3}$ . The experimentally measured magnetization dynamics for different orientations of an external magnetic field agrees well with numerical solutions of magnetoelastically driven magnon harmonic oscillators. Symmetry-based selection rules for magnon-phonon interactions predicted by our modeling approach allow for the unambiguous discrimination between spatially uniform and nonuniform modes, as confirmed by comparing the resonantly enhanced magnetoelastic dynamics simultaneously measured on opposite sides of the film. Moreover, the separation of timescales for (early) rising and (late) decreasing precession amplitudes provide access to magnetic (Gilbert) and acoustic damping parameters in a single measurement.

DOI: [10.1103/PhysRevB.107.134419](https://doi.org/10.1103/PhysRevB.107.134419)

**I. INTRODUCTION**

Since early experimental studies [1–3], ultrafast magnetoelastic interactions driven by femtosecond light pulses are conveniently described in the time domain: the dynamics of magnetization driven by single or multiple acoustic pulses with picosecond duration are monitored using the magneto-optical pump-probe technique. This intuitive picture allows for an elegant description of magnetization precession amplified by a sequence of acoustic pulses with an appropriate time interval via the magnetoacoustic coherent control mechanism [4,5]. Moreover, the time-domain picture of ultrafast magnetoacoustics facilitates the interpretation of magnetization switching [6,7], where the duration of acoustic pulses is shorter than the period of ferromagnetic resonance (FMR) precession.

An alternative view on ultrafast magnetoacoustics is provided in magneto-optical transient grating experiments [8–11]. Here, the spectrally separated quasimonochromatic acoustic excitations allow for observing resonant amplification of FMR precession induced by each acoustic mode. Such resonant amplification has also been observed in experimental setups involving ferromagnetic thin films embedded in acoustic cavities [12], deeply subwavelength ferromagnetic nanogratings [13], and nanomagnets [14]. In all these

experiments the dependence of the FMR frequency on the external magnetic field makes it possible to tune the FMR precession in resonance with a long-lived acoustic mode of interest. Very recently we have extended this approach to ultrafast magnetoacoustic dynamics in freestanding thin films and multilayers [15]. Our theoretical approach is based on eigenmodes decomposition of both acoustic and magnetization dynamics, which allows for a more insightful analysis of ultrafast magnetoacoustic dynamics experiments in terms of resonant magnetoelastic interactions between individual modes of longitudinal acoustic phonons and perpendicular standing-spin-wave (magnon) modes [16]. For instance, the application of such rigorous theoretical analysis to resonant phonon-magnon interactions in freestanding multilayer structures predicts the key role of the symmetry of magnetic and acoustic modes in prescribing well-defined selection rules for individual phonon-magnon interactions. One of the most relevant conclusions was that in symmetric structures interactions between magnon and phonon eigenmodes with different symmetries were forbidden.

In this paper, with the purpose of benchmarking the power of our improved approach, we apply it to reinterpreting the experimental results by Kim and Bigot [5] obtained for a 300-nm freestanding nickel thin film. We show that even for such thick structures, where frequencies of spatially uniform (FMR) and nonuniform (spin-wave or magnon) modes cannot be distinguished using conventional approaches employed so far, our approach enables the detection of their excitation thanks to the

\*vasily.temnov@cnrs.fr

symmetry-dependent selection rules that govern their resonant interaction with acoustic modes. The results of this work are multiple: from the one side they demonstrate the ability of our modeling to retrieve fundamental parameters governing the complex physics involved in ultrafast magnetoacoustic experiments with an unprecedented accuracy, and from the other side they corroborate that the physical picture embodied in our model is particularly insightful, for example, by highlighting the importance of symmetries in magnetoacoustics. Here we would like to stress that the original interpretation in Ref. [1] roots back to the analysis of the dynamics of the spatially homogeneous (FMR) mode excited by a sequence of acoustic pulses. This intrinsically different phenomenological time-domain approach did not allow for identification of spatially inhomogeneous modes (magnon modes) and made the extraction of magnetic (Gilbert) and acoustic damping constants extremely challenging, as partially explained in Sec. V.

## II. EXPERIMENT

Freestanding nickel membranes in the experiment in Ref. [5] had a thickness  $L = 300$  nm and were obtained by depositing Ni on a glass substrate with a layer of sodium chloride in between them. The layer was subsequently dissolved in water to leave the Ni film stretched on a sample holder with a hole. The film was stretched laterally by gluing a silver paste around the edges of the film, which created a static strain in nickel upon drying out.

The nickel thin film was optically excited at the front side by a femtosecond pump pulse (400-nm wavelength, 45-fs pulse duration, 10-kHz repetition rate,  $1.5$  mJ/cm<sup>2</sup> fluence), launching pulses of coherent longitudinal acoustic phonons with a duration of a few picoseconds propagating inside the sample at a constant speed  $c_s = 6$  nm/ps [see Fig. 1(a)]. Due to the inverse magnetostrictive effect, these acoustic pulses drove the magnetization dynamics inside the Ni film. Time-delayed probe pulses of 800 nm detected transient changes in the reflectivity and magneto-optical Kerr effect (MOKE) rotation, both at the front and back sides of the sample. A rotating permanent magnet positioned on top of the sample produced a magnetic field with reported magnitude  $\mu_0 H \sim 0.4$  T at a variable angle  $\xi$  with respect to the surface normal. Due to the magnetic anisotropy the equilibrium direction of magnetization was noncollinear with the external magnetic field and made an angle  $\theta$  with the surface normal.

Figure 1(b) shows the measured differential reflectivity  $\frac{\Delta R}{R}$  and Kerr rotation  $\psi$  at the back side of the film for five different orientations of the external magnetic field:  $\xi = 15.5^\circ, 26^\circ, 35^\circ, 46.5^\circ,$  and  $65^\circ$ . The slowly varying thermal background in reflectivity and Kerr rotation signals originated from heat diffusion from the front to the back side of the film and will be subtracted throughout the manuscript in order to facilitate the quantitative comparison with simulations of rapidly varying elastic and magnetoelastic transients. Complementary Kerr rotation and reflectivity measurements were performed at the front side of the film: these data are introduced and discussed in Fig. 2(a) for reflectivity and Fig. 4(a) for Kerr rotation.

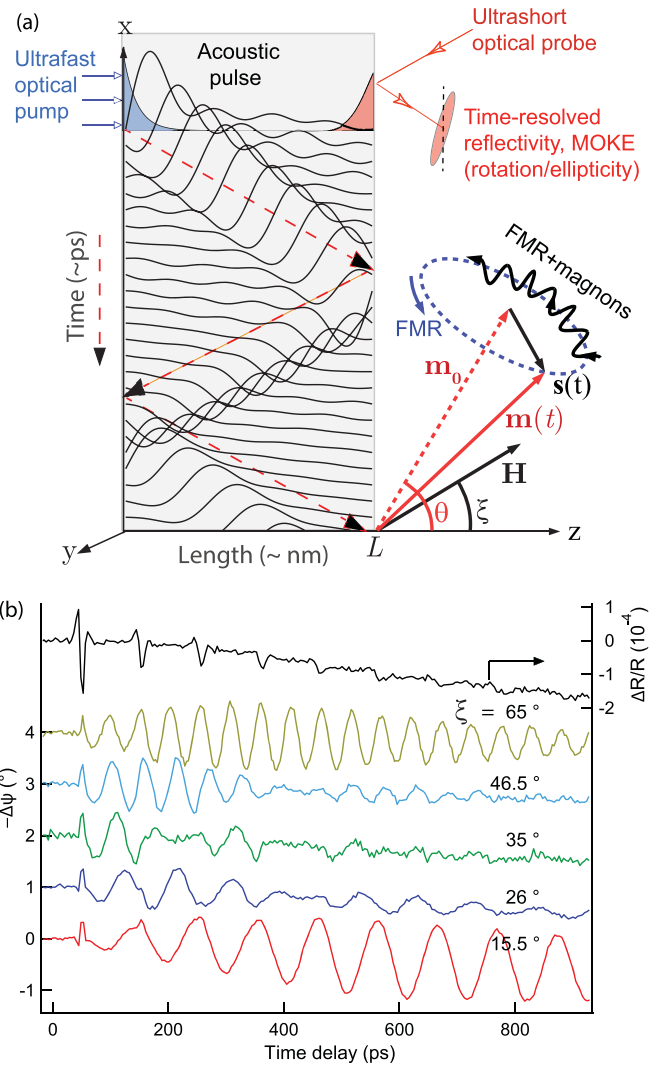


FIG. 1. (a) Schematic picture of the experiment and acoustic pulse propagating inside the sample. The shaded exponentially decaying functions illustrate the optical penetration depth of pump and probe pulses, respectively. (b) Experimental data for reflectivity and Kerr rotation.

## III. PHYSICAL MODEL

Excitation of acoustic and magnetic transients in ferromagnetic nickel with femtosecond laser pulses can be adequately described by the phenomenological two-temperature model (TTM) [17], which governs the phenomena of ultrafast demagnetization on a deeply sub-picosecond timescale [18,19] and generation of ultrashort acoustic pulses on a picosecond timescale [20]. In the current paper, we are going to disregard the phenomenon of transient ultrafast demagnetization and focus on the *resonantly enhanced interactions* between the long-living femtosecond-laser-generated acoustic transients and the magnetization dynamics, an effect that dominates contributions from ultrafast demagnetization reported in nickel thin films on silicon substrates [16].

Within the framework of the TTM, the nonequilibrium hot electrons are initially generated through the absorption of an optical pump pulse within its skin depth. Subsequently, they

transport energy into the depth of the sample via electron diffusion and heat up the cold lattice via electron-phonon scattering. These complex spatiotemporal dynamics result in the emission of picosecond acoustic pulses caused by the thermal expansion of rapidly heated lattice. In the case of a freestanding nickel film, these acoustic pulses generated at the front side of the sample, propagate through the film, are reflected at the back Ni/air interface (with a reflection coefficient equal to -1), and keep bouncing back and forth between these two interfaces before they decay due to various phonon scattering mechanisms.

The magnetization dynamics induced by such ultrashort acoustic pulses can be adequately described by a phenomenological approach using magnetoelastically driven Landau-Lifshitz-Gilbert (LLG) equations [1–3]. Adapted to the experimental geometry in Fig. 1, the phenomenological free energy density  $F = F_Z + F_d + F_{ex} + F_{me}$  takes into account the Zeeman term  $F_Z = -\mu_0 M_0 \mathbf{m} \cdot \mathbf{H}$  due to the presence of the external magnetic field  $\mathbf{H}$ , the anisotropy energy  $F_d = (\frac{1}{2}\mu_0 M_0^2 + K)m_z^2$  consisting of the thin-film shape anisotropy, and the phenomenological anisotropy constant  $K$  due to static built-in strains in a stretched nickel membrane, the exchange energy  $F_{ex} = \frac{1}{2}M_0^2 \sum_{i=1}^3 D(\frac{\partial \mathbf{m}}{\partial x_i})^2$ , and the magnetoelastic energy  $F_{me}(t) = b_1 m_z^2 \varepsilon_{zz}(z, t)$  ( $b_1 \simeq 10^7$  J/m<sup>3</sup> for nickel [21]) due to the interaction with an acoustic pulse  $\varepsilon_{zz}(z, t)$ . The relation between the angle  $\xi$  of the magnetic field and  $\theta$  magnetization at equilibrium is given by

$$\sin(\theta - \xi) = \frac{\tilde{M}}{2H} \sin 2\theta, \quad (1)$$

where  $\tilde{M} = M_0 + \frac{2K}{\mu_0 M_0}$ , and  $M_0$  is the saturation magnetization for Ni. The length of the magnetization vector stays constant in our model (assuming constant temperature), so

$$\frac{d^2 s_z^{(n)}}{dt^2} + 2\alpha\omega_n \frac{ds_z^{(n)}}{dt} + \omega_n^2 s_z^{(n)} = f_n(t), \quad (4)$$

where  $\alpha$  is the Gilbert damping parameter and magnon eigenfrequencies  $\omega_n$  obey

$$\omega_n = \gamma\mu_0\sqrt{[H \cos \xi - (\tilde{M} - \tilde{D}k_n^2) \cos \theta]^2 + (H \sin \xi + \tilde{D}k_n^2 \sin \theta)[H \sin \xi + (\tilde{M} + \tilde{D}k_n^2) \sin \theta]}. \quad (5)$$

Here  $\tilde{D} = D/(\hbar\gamma\mu_0)$  is the exchange stiffness ( $D = 430$  meV Å<sup>2</sup> from Ref. [16]), and  $\gamma$  denotes the gyromagnetic ratio.

The external magnetoelastic driving force,

$$f_n(t) = P_n(\mathbf{H}) \int_0^L \varepsilon_{zz}(z, t) \cos(k_n z) dz, \quad (6)$$

is proportional to the overlap integral between the magnon eigenmode with the acoustic strain pulse  $\varepsilon_{zz}(z, t)$ . For our experimental geometry the prefactor

$$P_n(\mathbf{H}) = \frac{\mu_0 \gamma^2 b_1 \sin(2\theta)(\tilde{D}k_n^2 \sin \theta + H \sin \xi)}{M_0 L} \quad (7)$$

is proportional to the magnetostriction coefficient  $b_1$  and depends both on the magnitude and orientation of an external magnetic field  $\mathbf{H}$ .

Understanding the magnetoelastic dynamics governed by Eq. (4) is facilitated by decomposing the acoustic strain pulse

the magnetization dynamics can be described with the unit magnetization vector  $\mathbf{m}$  and its precession  $\mathbf{s}(z, t)$ :

$$\mathbf{m} = \mathbf{m}_0 + \mathbf{s}(z, t), \quad (2)$$

which can be represented as a sum of magnetic eigenmodes:

$$\mathbf{s}(z, t) = \sum_{n=0}^{\infty} \mathbf{s}^{(n)}(t) \cos(k_n z), \quad (3)$$

where  $k_n = \pi n/L$  is the wave vector of the  $n$ th magnetic eigenmode and free boundary conditions for magnetization dynamics are assumed. The  $n = 0$  magnetic eigenmode with a uniform spatial profile corresponds to FMR, while higher-order  $n \geq 1$  modes describe spatially nonuniform modes of exchange magnons.

Whereas the role of magnetic boundary on magnetoacoustic interactions has been discussed in Ref. [22], here we assume the commonly used free boundary conditions for magnetization at Ni/air interfaces [16,23]. However, the results of our analysis remain valid even in case of pinned and mixed boundary conditions if the latter are identical at both Ni/air interfaces. In this case (i) the symmetry of magnetic eigenmodes does not depend on the nature of boundary conditions, i.e., the conclusion about the magnetoelastic selection rules between phonon and magnon modes holds, and (ii) magnon frequencies will experience only minor changes because of a thick nickel layer.

It has been shown [15,24] that in the linear approximation when the acoustic strains are small, the magnetoelastically driven dynamics for each magnon mode satisfy the equation of a damped driven harmonic oscillator,

in its eigenmodes according to

$$\varepsilon_{zz}(z, t) = \sum_{p=1}^{\infty} \varepsilon_{zz}^{(p)}(z) e^{-\gamma_p t} \cos(\omega_p t + \varphi_p). \quad (8)$$

We assume acoustic eigenmodes to oscillate at frequencies  $\omega_p = c_s k_p$  and decay with damping constants  $\gamma_p$ ;  $\varphi_p$  denote their initial phases. In a freestanding film, the acoustic eigenmodes obey the free boundary conditions for the acoustic displacement (corresponding to zero strains at both Ni/air interfaces), resulting in

$$\varepsilon_{zz}^{(p)}(z) = a_p \sin(k_p z), \quad (9)$$

where  $k_p = \pi p/L$  is the wave vector of the  $p$ th acoustic eigenmode. Using the decomposition of the acoustic strain in its respective eigenmodes, the expression of the magnetoelastic

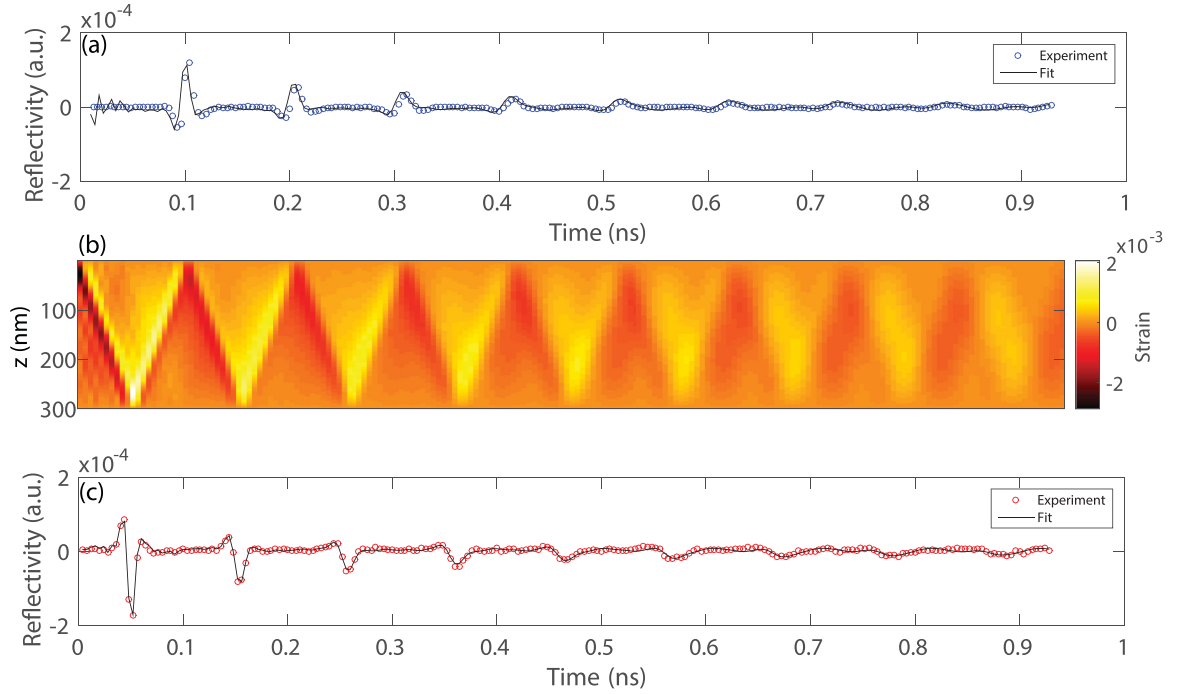


FIG. 2. (a) Experimentally measured reflectivity at the front side of the Ni film, superimposed with its fit as a superposition of ten decaying sinusoidal eigenmodes. (b) Color map showing the reconstituted strain inside the film as a function of position and time. (c) Experimental reflectivity measurement at the back side of the Ni film, together with its fit.

driving force becomes

$$f_n(t) = P_n(\mathbf{H}) \sum_{p=1}^{\infty} I_{np} a_p e^{-\gamma_p t} \cos(\omega_p t + \varphi_p). \quad (10)$$

Here we have introduced the overlap integral [15]

$$I_{np} = \int_0^L \cos(k_n z) \sin(k_p z) dz \quad (11)$$

between the  $n$ th magnetic and  $p$ th acoustic eigenmodes.

To sum up this section, after having quantified the acoustic strain and decomposed it in its eigenmodes, we can use Eqs. (4)–(5) and (10)–(11) to simulate the time evolution of the magnetization precession. To solve Eq. (4) numerically, we use the fourth-order Runge-Kutta method.

#### IV. ANALYSIS OF ACOUSTIC DATA

The change in reflectivity measured by the probe pulse after excitation with the pump pulse is related to the strain inside the film through the sensitivity function  $f(z)$ , which depends on the optical constants of Ni. Their relation (as in [25]) is given by

$$\frac{\Delta R(t)}{R} = 2\text{Re}\left(\frac{\Delta r(t)}{r}\right) = \int_0^L \varepsilon_{zz}(z, t) f(z) dz, \quad (12)$$

where we used the expression for the sensitivity function in the complex notation [20]:

$$f(z) = \frac{16\pi}{\lambda} \text{Re}\left(i \frac{\partial \tilde{n}}{\partial \varepsilon_{zz}} \frac{\tilde{n}}{\tilde{n}^2 - 1} e^{i \frac{4\pi \tilde{n}}{\lambda} z}\right). \quad (13)$$

Here  $\tilde{n} = 2.48 + 4.38i$  denotes the complex index of refraction of Ni at the probe wavelength  $\lambda = 800$  nm, and its derivative with respect to the applied strain  $\frac{\partial \tilde{n}}{\partial \varepsilon_{zz}} = 0.6 - 1.8i$  [20] is called the photoelastic coefficient. The spatial dependence of the sensitivity function is dominated by the exponential decay  $\propto \exp(-z/\delta_{skin})$  within the optical penetration depth of the probe pulse  $\delta_{skin} = \frac{\lambda}{4\pi \text{Im}(\tilde{n})} = 14.5$  nm.

Using the previous decomposition of strain into eigenmodes, we obtain the following expression for the measured reflectivity:

$$\frac{\Delta R(t)}{R} = \sum_{p=1}^{\infty} a_p J_p e^{-\gamma_p t} \cos(\omega_p t + \varphi_p), \quad (14)$$

where we can interpret  $J_p = \int_0^L f(z) \sin(k_p z) dz$  as the detection integral of the  $p$ th mode. This expression for the transient reflectivity shows that it can be represented as a sum of damped harmonic oscillations, suggesting that the Fourier transform of the signal could be useful in characterizing the acoustic eigenmodes. Panels (a) and (c) in Fig. 2 show the reflectivity signal at the front and back side of the film, while Fig. 3(a) displays the Fourier transform of the back-side reflectivity signal. The data allows us to distinguish ten peaks in the Fourier transform, so we carry out the analysis using the first ten acoustic modes.

To obtain the amplitudes, lifetimes, and phases of the respective acoustic modes, we performed a nonlinear least-squares fitting (using the Levenberg-Marquardt algorithm) of the reflectivity data at the back side with Eq. (14), where  $a_p$ ,  $\gamma_p$ , and  $\varphi_p$  are taken as fit parameters and frequencies  $\omega_p$  are extracted from the Fourier spectrum. Initial guesses for the

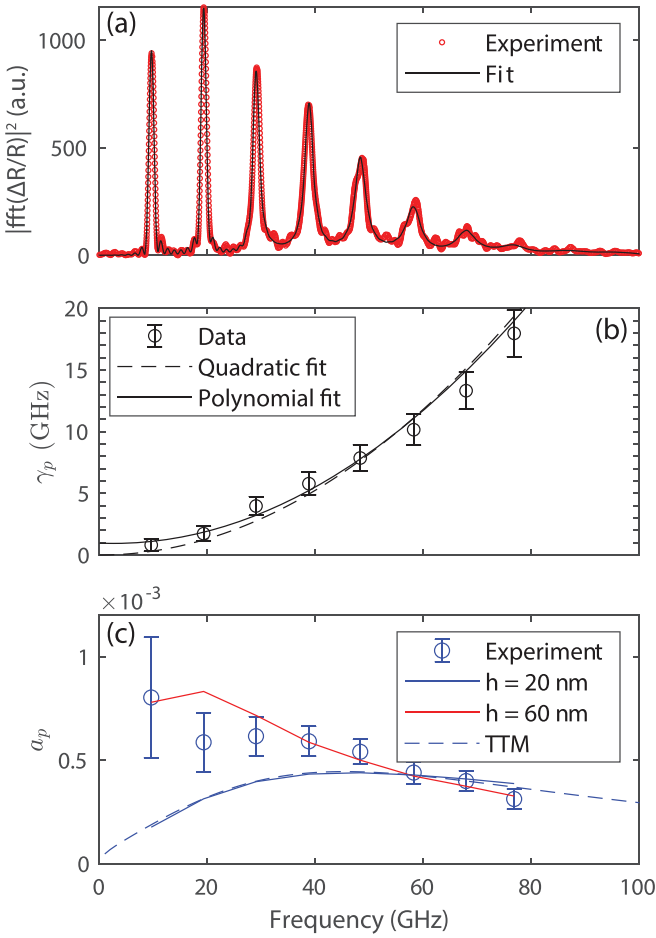


FIG. 3. (a) Fourier power spectrum of the experimental reflectivity and of its fit, for the back side of the film. (b) Damping as a function of frequency, as extracted from the fitting procedure. The result follows a quadratic law to a very good approximation. (c) Amplitudes of the acoustic modes, as extracted from the fitting procedure. The dashed line represents the acoustic frequency spectrum according to Eq. (5) in Ref. [20] for nickel thin films excited by weak fs pump pulses, amplitudes obtained with Eq. (15) assuming exponential heating profiles with  $h = 20$  nm and 60 nm are shown for comparison (continuous lines).

values of  $a_p$ ,  $\gamma_p$ , as well as estimations of the resulting error bars are obtained by manually fitting the Fourier power spectrum in Fig. 3(a) with a superposition of Lorentzian curves centered around the acoustic eigenfrequencies  $f_p = \omega_p/(2\pi)$  and characterized by the (FWHM) width  $\Delta f_p = \gamma_p/\pi$ . The results of such fitting in Figs. 2(a), 2(c) and 3(a) appear to be in an excellent agreement with experimental data.

Furthermore, panels (b) and (c) in Fig. 3 show the dependence of damping and amplitudes for the first eight eigenmodes on their frequencies. The second-degree polynomial fit of damping  $\gamma_p$  as a function of frequency shows that the quadratic term dominates. Thus we can conclude that damping scales quadratically with frequency up to around 80 GHz. This result is consistent with Ref. [26], suggesting that the attenuation mechanism is due to the phonon-phonon scattering.

The straightforward attempt to understand the fitted amplitudes [Fig. 3(c)] within the framework of the TTM failed.

Using Eq. (5) and the set of experimental fit parameters in the low-fluence excitation regime (pump fluence  $\sim 0.01$  mJ/cm<sup>2</sup>) in nickel thin films [20] results in the initial heat penetration depth  $h = 20$  nm that only slightly exceeds the optical skin depth of our pump pulses. In terms of the acoustic amplitudes, the results of the TTM are well approximated by a simplified phenomenological model assuming an instantaneous heating with an exponential profile  $\propto \exp(-z/h)$ , giving rise to

$$a_p \propto \int_0^L e^{-z/h} \sin(k_p z) dz. \quad (15)$$

The strong disagreement between the theory and the experimental data indicates that this modeling cannot be applied. In the strong-excitation regime used in this experiment, the parameters of the two-temperature model display strong dependence on the pump fluence [27], resulting in larger electronic heat capacity and weaker electron-phonon coupling. Both effects favor a larger heat penetration depth mediated by hot electron diffusion during the increase electron-phonon relaxation time. We can account for this effect by assuming a larger heat penetration depth  $h = 60$  nm, which provides a better approximation to the experimental data. However, it is clear that the discussed theoretical models represent oversimplifications and a further systematic study of the strong-excitation regime of picosecond acoustic pulses is necessary.

Using the obtained amplitudes, phases, and damping parameters, we can reconstruct the strain inside the film as a function of space and time. Figure 2(b) shows an evolution of spatial strain that is in accordance with the intuitive image of an acoustic echo propagating back and forth, undergoing reflections at both ends of the film and damping in time. But in addition to this intuitive picture, the eigenmode decomposition also helps in explaining the broadening of acoustic echo in the time domain, which is due to the frequency-dependent damping.

## V. ANALYSIS OF MAGNETIZATION DYNAMICS

Magnetization dynamics in the Ni film are analyzed by measuring the Kerr rotation angle. The depth sensitivity function of MOKE becomes important in the case of ultrafast magnetization dynamics, varying within the skin depth of light due to the presence of spatially nonuniform high-frequency magnons. The relation between the detected Kerr rotation and the magnetization precession  $s_z(z, t)$  inside the film is given by

$$\frac{\Delta\psi(t)}{\psi_s} = \int_0^L s_z(z, t) g(z) dz, \quad (16)$$

where  $\psi_s$  is the static Kerr rotation angle,  $\Delta\psi(t)$  is its change due to magnetization precession, and  $g(z)$  is the depth sensitivity function for the polar MOKE [28]:

$$g(z) = \frac{4\pi}{\lambda} \text{Re} \left( i Q_{MO} \frac{\tilde{n}^2}{1 + \tilde{n}^2} e^{-i \frac{4\pi \tilde{n}}{\lambda} z} \right). \quad (17)$$

Here, unlike the acoustical sensitivity function, the magneto-optical response is valued by the complex magneto-optical (Voigt) constant  $Q_{MO} = i \frac{\tilde{\epsilon}_{xy}}{\tilde{\epsilon}_{xx}} = -(4.9 + 10.5i) \times 10^{-3}$  [29].

Using our previous decomposition in magnon eigenmodes, we get an expression that ties the dynamics of individual

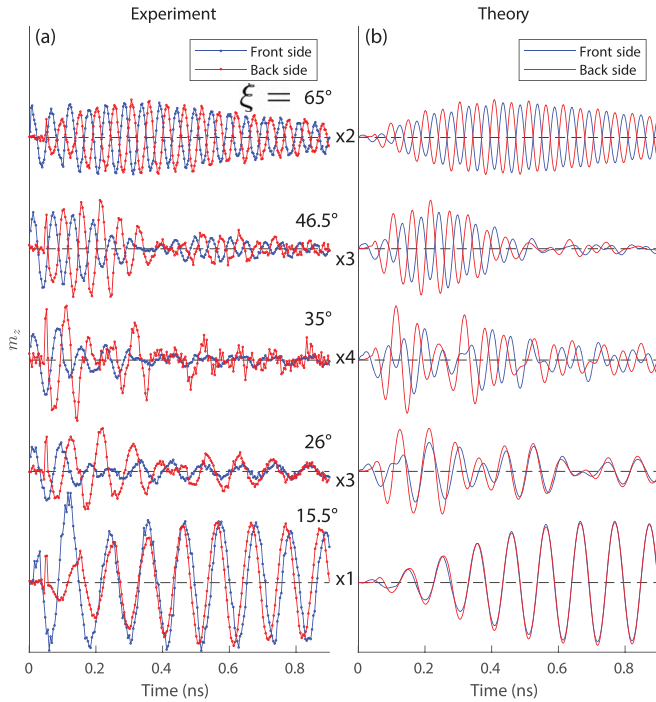


FIG. 4. Comparison of magnetization dynamics at the front and back side of the film, as obtained (a) experimentally and (b) from our simulations. For lower-amplitude signals multipliers are used, the values of which are indicated next to the curves.

magnon modes to the Kerr rotation:

$$\frac{\Delta\psi(t)}{\psi_s} = \sum_{n=0}^{\infty} \tilde{J}_n s_z^{(n)}(t), \quad (18)$$

where  $\tilde{J}_n = \int_{z=0}^L g(z) \cos(k_n z) dz$  is the detection integral of the  $n$ th magnon mode. Using this expression we can fit the results of our magnetization dynamics simulation with those of the experiment in the next section.

## VI. RESONANT PHONON-MAGNON INTERACTIONS

The experimental data for the back- and front-side Kerr rotation are presented in Fig. 4(a) for different orientations of the external magnetic field. We simulate the Kerr rotation by solving Eq. (4) for each magnon and using the sensitivity function defined in the previous section to obtain the Kerr rotation from Eq. (18). In order to reach an agreement with experimental data for all angles  $\xi$  in Fig. 4, we have used the values for the anisotropy constant  $K$ , magnitude of the magnetic field  $H$ , and Gilbert damping  $\alpha$  as fit parameters. Using the magnetic field of 0.3 T, the anisotropy constant  $K = 2.05 \times 10^5$  J/m<sup>3</sup>, and the Gilbert damping  $\alpha = 0.04$ , we achieve the quantitative agreement between the experimental data and simulations (Fig. 4). The value of the magnetic field stays within the expected error bar for a permanent magnet placed on top of the sample. The value of the Gilbert damping is equal to the one obtained in a recent study of ultrafast magnetization dynamics in nickel nanomagnets [14]. The simulated Kerr rotation at the front and back sides are represented in Figs. 4(a) and 4(b). We observe an excellent agreement

between the experimental data and simulations, except for the initial thermal excitation of magnetization at the front side, which we did not account for in our model and which acts only at early times.

Given this agreement between experimental data and simulations, we analyze the peculiarities of the magnetization dynamics at different angles. For 15.5°, the magnetization dynamics at the back side is in phase with that at the front side, while for 65° they are  $\pi$ -shifted. Moreover, we notice that the magnetization precession at 15.5° and 65° lasts longer and is stronger than at other angles. While at 15.5° and 65° there are some slowly varying long-lived dynamics, at angles 26°, 35°, and 46.5° we observe weak, somewhat irregular beating patterns.

A complementary perspective is presented in Fig. 5, which shows the reconstructed magnetization dynamics inside the sample [Figs. 5(b) and 5(c)] as a function of position and time. After the transient regime dies out, the magnetization profile for 15.5° is approximately uniform in space, suggesting that the dynamics is dominated by the FMR ( $n = 0$ ) mode. On the other hand, the dynamics at 65° follow the spatially antisymmetric profile with respect to the middle of the film, which suggests that in this configuration the  $n = 1$  magnon dominates. This conclusion is in line with the observed  $\pi$ -phase shift between the data at the front and the back side at 65°, see Fig. 4. At an intermediate angle of 35°, the magnetization dynamics with a much smaller amplitude are mainly visible at early delay times. This suggests that in this intermediate regime no magnon modes are resonantly excited.

All these observations can be explained by a simple theory for a driven harmonic oscillator. The main result is that the oscillation amplitude is resonantly enhanced when the natural frequency (here, that of magnons  $\omega_n$ ) equals the driving frequency (in our case, that of phonons  $\omega_p$ ). Away from resonance, the transient regime is characterized by a beating pattern because of the difference between the natural and driving frequencies.

Figure 5(a) shows the amplitude of magnetization precession as a function of its frequency and the angle of the external magnetic field. Two bright spots are visible: one at the point where the frequency of the first phonon ( $p = 1$ ) matches that of FMR ( $n = 0$ ) and another one where the frequency of the second phonon ( $p = 2$ ) matches that of the first magnon ( $n = 1$ ).

However, for our symmetric freestanding membrane the overlap integral  $I_{np}$  (Fig. 6) is zero when the acoustic modes possess a different symmetry from that of the magnon modes. This means that symmetric (antisymmetric) acoustic modes will interact only with symmetric (antisymmetric) magnon modes, respectively. Therefore, the symmetry-based selection rules become as important for resonant phonon-magnon interaction as the previously mentioned frequency-matching condition.

These considerations enable us to identify the driving forces of the magnetization dynamics observed at the three angles shown in Fig. 5. At 15.5°, the frequency of the first phonon ( $p = 1$ ) matches that of the first few magnons but the symmetry of the modes allows only even magnons to be excited. Since the overlap integral decays with increasing magnon number, the dominant magnetic mode at 15° is the

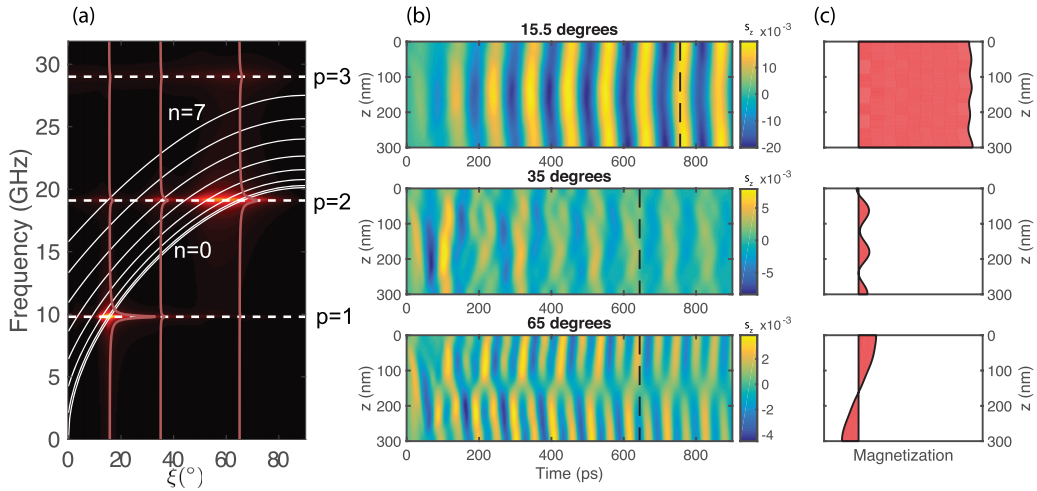


FIG. 5. (a) Fourier transform of simulated Kerr rotation as a function of magnetic field angle. The dashed lines indicate the frequencies of phonons, and the continuous white lines are the dispersion curves of magnons. Vertical cross sections into the heat map, corresponding to the three angles in panel (b), are shown. (b) Magnetization dynamics inside the film, as a function of position and time, for three experimental angles. (c) Magnetization profiles, taken at the times indicated in panel (b) by dashed lines.

FMR ( $n = 0$ ). At  $65^\circ$ , the second phonon ( $p = 2$ ), whose frequency matches the frequencies of the first few magnons, interacts only with odd magnons. Thus the dominant mode in this case is the first magnon ( $n = 1$ ). At  $35^\circ$ , the magnon frequencies are between the frequency of the first ( $p = 1$ ) and second ( $p = 2$ ) phonon and exhibit no resonant interaction. Hence, the magnetization precession is significantly weaker.

Figure 7 illustrates the quantitative agreement between the theory and the experiment for the two resonantly driven magnetization dynamics. Qualitative analysis suggests that in both

cases the dynamics can be described by the rise time  $\tau_{\text{rise}}$  and decay time  $\tau_{\text{decay}}$ . The magnetization dynamics can be well approximated by a phenomenological envelope function

$$A(t) \propto (1 - e^{-t/\tau_{\text{rise}}})e^{-t/\tau_{\text{decay}}}. \quad (19)$$

For the magnetization dynamics at  $15.5^\circ$ , the characteristic rise time is  $\tau_{\text{rise}}^{(1)} = 0.62$  ns and the decay time is  $\tau_{\text{decay}}^{(1)} = 1.13$  ns. Similarly, for the second resonance at  $65^\circ$  we extract  $\tau_{\text{rise}}^{(2)} = 0.35$  ns and  $\tau_{\text{decay}}^{(2)} = 0.45$  ns, respectively.

In order to interpret the observed rise and decay times we have solved Eq. (4) analytically, assuming that it is driven by a single acoustic mode  $\propto e^{-\beta\omega_p t} \cos \omega_p t$  at resonance, i.e.,  $\omega_p = \omega_n = \omega$ ; the acoustic damping is written as  $\gamma_p = \beta\omega_p$ . The approximate solution for the envelope function reads

$$A(t) \propto |e^{-\alpha\omega t} - e^{-\beta\omega t}|, \quad (20)$$

where we have assumed  $\alpha \neq \beta \ll 1$  and neglected small terms  $\propto \alpha^2, \beta^2, \alpha\beta$  and higher powers. Equation (20) is equivalent to Eq. (19) with the rise and decay times given by

$$\tau_{\text{rise}} = \frac{1}{|\alpha - \beta|\omega} \quad (21)$$

and

$$\tau_{\text{decay}} = \max\left(\frac{1}{\alpha\omega}, \frac{1}{\beta\omega}\right), \quad (22)$$

respectively. From the symmetry of these equations with respect to the permutation of  $\alpha$  and  $\beta$ , it is obvious that some additional information is needed to identify the Gilbert damping  $\alpha$  and acoustic damping  $\beta$ . For example, in the case of the first resonance in Fig. 7(a), one of the possibilities would be to have ( $\alpha_1 = 0.014, \beta_1 = 0.04$ ). However, this pair of parameters corresponds to an unreasonably low value for Gilbert damping for nickel and leads to the large value of acoustic damping  $\gamma_1 = 2.4$  GHz, in contradiction with results in Fig. 3(b). The second possibility ( $\alpha_1 = 0.04, \beta_1 = 0.014$ ) provides both the commonly accepted values for nickel [14,16] and the acoustic linewidth of 1 GHz in agreement with

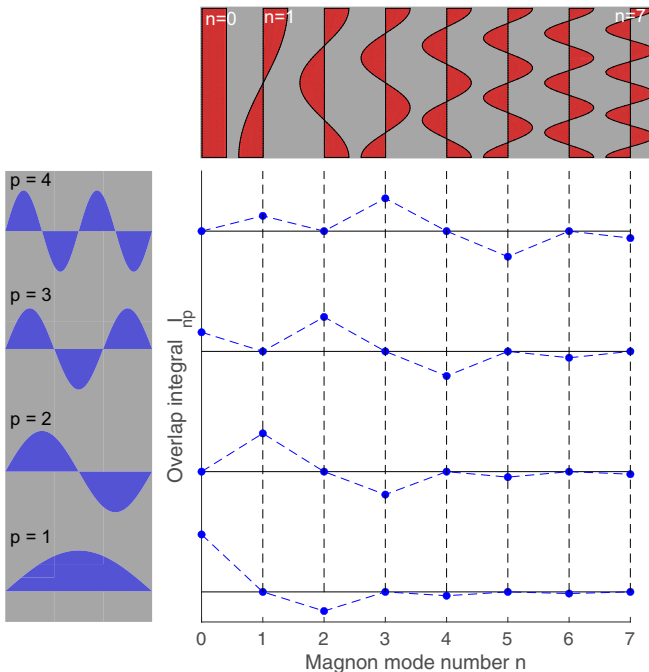


FIG. 6. Representation of magnonic eigenmodes (along the horizontal axis) and acoustic eigenmodes (along the axis) with their corresponding overlap integrals.

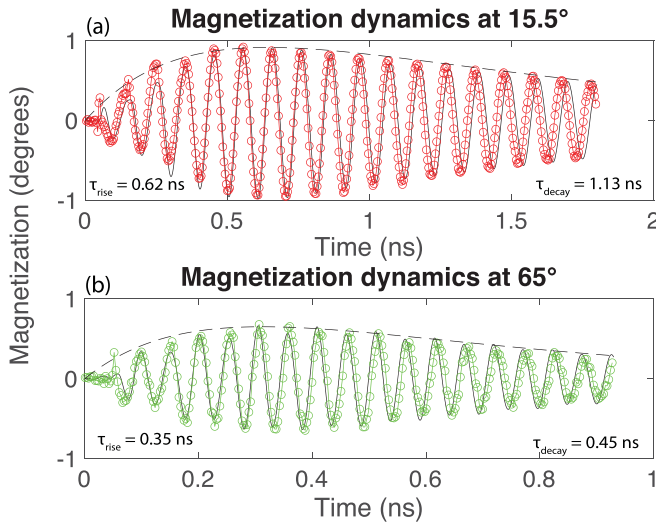


FIG. 7. Long-scan magnetization dynamics at the back side of the film, under the magnetic field angles (a)  $\xi = 15.5^\circ$  and (b)  $\xi = 65^\circ$ . Experimental data is represented by dots, the simulated curve is a black continuous line, while the dashed curve denotes the fit envelope  $A(t)$ . The separation of timescales is clearly visible in both graphs: the initial growth governed by the Gilbert damping is followed by the decay due to the acoustic decay.

Fig. 3(b). Similar arguments apply to the second resonance in Fig. 7(b) quantified with ( $\alpha_2 = 0.041$ ,  $\beta_2 = 0.018$ ). Therefore we conclude that the independent quantitative characterization of acoustic lifetimes is indispensable for the correct physical interpretation of acoustically induced magnetization dynamics in the time domain [5].

The previous discussion can be reformulated in terms of quality factors of magnon and phonon resonances. The magnon quality factor  $Q_G = 1/(2\alpha) \simeq 12$  does not depend on the mode number, in agreement with previously reported results on frequency-independent Gilbert damping  $\alpha$  [23,30]. Acoustic quality factors  $Q_{ac}^{(1)} = 1/(2\beta_1) \simeq 36$  and  $Q_{ac}^{(2)} = 1/(2\beta_2) \simeq 28$  are slightly different due to the observed nonlinear dependence of acoustic damping on frequency, converging to the approximate scaling  $Q_{ac}(\omega) \propto \omega^{-1}$  for higher-order acoustic modes. The observed high values of acoustic quality factors  $Q_{ac} > Q_G$  enable the separation of timescales in the excitation and decay phases in the magnetization dynamics.

Qualitatively similar magnetization dynamics have been observed earlier in transient grating experiments [8]. However, in the latter case the conspicuous decay of magnetization dynamics was explained by the complex spatiotemporal dynamics of the magnitude of the magnetization vector  $M_z(x, t)$  on the temperature  $T(x, t)$  in the periodically demagnetized nickel film [9,11]. In this context, our experimental geometry

probing the magnetization dynamics at the back side of the sample provides an advantage of isolating resonant phonon-magnon interactions from thermal effects and extracting their properties from the same measurement.

## VII. SUMMARY AND CONCLUSIONS

In this manuscript we reported on the quantitative analysis of experimental data by Kim and Bigot in a freestanding nickel thin film [5] based on the decomposition of magnetic and acoustic dynamics in phonon and magnon eigenmodes, respectively. The time-domain fitting of transient reflectivity data on both sides of the nickel film provides frequencies, lifetimes, and phases of individual acoustic eigenmodes. The latter is shown to drive the magnetization dynamics to be in quantitative agreement with time-resolved MOKE measurements. Notably, the comparison of MOKE signals on both sides of the sample evidence the in-phase FMR dynamics ( $n = 0$ , with minor contributions of symmetric magnon eigenmodes  $n = 2, 4, \dots$ ) induced by the lowest order ( $p = 1$ ) symmetric acoustic mode and the opposite-sign magnetization oscillation of antisymmetric magnon modes ( $n = 1, 3, \dots$ ). Being in a quantitative agreement with a simple theoretical model with tabulated material parameters, the experimental data clearly evidence the resonantly enhanced excitation of nonuniform magnon modes. Moreover, accurate fitting of the magnetization dynamics driven by long-lived  $p = 1$  (9.8 GHz) and  $p = 2$  (19.1 GHz) acoustic modes delivers the correct value for magnetic Gilbert damping  $\alpha = 0.04$ , corresponding to the quality factor  $Q_m = 12$  for magnon modes. Being smaller than the quality factors of acoustic modes, this magnetic quality factor assures optimum conditions for resonant phonon-magnon excitation, the phenomenon to be further explored in the ultrahigh-THz frequency regime [15,31].

## ACKNOWLEDGMENTS

We thank J.-Y. Bigot (deceased) in whose labs the reported measurements were performed. The support of the Physics Department of École Polytechnique and Institut Polytechnique de Paris within the framework of a *Projet de Recherche en Laboratoire* and by the ANR-21-MRS1-0015-01 “IRON-MAG” is gratefully acknowledged. P.V. acknowledges support from the Spanish Ministry of Science and Innovation and the European Union under the Maria de Maeztu Units of Excellence Programme (CEX2020-001038-M) and Project No. PID2021-123943NB-I00 (MICINN/FEDER). J.K. acknowledges support from the Basic Science Research Program through the National Research Foundation of Korea (NRF) funded by the Ministry of Education (2022R111A3072023) and by the MSIT (2021R1A4A1031920).

- [1] A. V. Scherbakov, A. S. Salasyuk, A. V. Akimov, X. Liu, M. Bombeck, C. Brüggemann, D. R. Yakovlev, V. F. Sapega, J. K. Furdyna, and M. Bayer, *Phys. Rev. Lett.* **105**, 117204 (2010).  
 [2] J.-W. Kim, M. Vomir, and J.-Y. Bigot, *Phys. Rev. Lett.* **109**, 166601 (2012).

- [3] L. Thevenard, E. Peronne, C. Gourdon, C. Testelin, M. Cubukcu, E. Charron, S. Vincent, A. Lemaître, and B. Perrin, *Phys. Rev. B* **82**, 104422 (2010).  
 [4] J.-W. Kim, M. Vomir, and J.-Y. Bigot, *Sci. Rep.* **5**, 8511 (2015).  
 [5] J.-W. Kim and J.-Y. Bigot, *Phys. Rev. B* **95**, 144422 (2017).

- [6] O. Kovalenko, T. Pezeril, and V. V. Temnov, *Phys. Rev. Lett.* **110**, 266602 (2013).
- [7] V. S. Vlasov, A. M. Lomonosov, A. V. Golov, L. N. Kotov, V. Besse, A. Alekhin, D. A. Kuzmin, I. V. Bychkov, and V. V. Temnov, *Phys. Rev. B* **101**, 024425 (2020).
- [8] J. Janušonis, C. L. Chang, T. Jansma, A. Gatilova, V. S. Vlasov, A. M. Lomonosov, V. V. Temnov, and R. I. Tobey, *Phys. Rev. B* **94**, 024415 (2016).
- [9] J. Janušonis, T. Jansma, C. L. Chang, Q. Liu, A. Gatilova, A. M. Lomonosov, V. Shalagatskyi, T. Pezeril, V. V. Temnov, and R. I. Tobey, *Sci. Rep.* **6**, 29143 (2016).
- [10] C. L. Chang, A. M. Lomonosov, J. Janusonis, V. S. Vlasov, V. V. Temnov, and R. I. Tobey, *Phys. Rev. B* **95**, 060409(R) (2017).
- [11] C. L. Chang, S. Mieszczak, M. Zelent, V. Besse, U. Martens, R. R. Tamming, J. Janusonis, P. Graczyk, M. Münzenberg, J. W. Klos, and R. I. Tobey, *Phys. Rev. Appl.* **10**, 064051 (2018).
- [12] J. V. Jäger, A. V. Scherbakov, B. A. Glavin, A. S. Salasyuk, R. P. Champion, A. W. Rushforth, D. R. Yakovlev, A. V. Akimov, and M. Bayer, *Phys. Rev. B* **92**, 020404(R) (2015).
- [13] A. S. Salasyuk, A. V. Rudkovskaya, A. P. Danilov, B. A. Glavin, S. M. Kukhtaruk, M. Wang, A. W. Rushforth, P. A. Nekludova, S. V. Sokolov, A. A. Elistratov, D. R. Yakovlev, M. Bayer, A. V. Akimov, and A. V. Scherbakov, *Phys. Rev. B* **97**, 060404(R) (2018).
- [14] C. Berk, M. Jaris, W. Yang, S. Dhuey, S. Cabrini, and H. Schmidt, *Nat. Commun.* **10**, 2652 (2019).
- [15] U. Vernik, A. M. Lomonosov, V. S. Vlasov, L. N. Kotov, D. A. Kuzmin, I. V. Bychkov, P. Vavassori, and V. V. Temnov, *Phys. Rev. B* **106**, 144420 (2022).
- [16] M. van Kampen, C. Jozsa, J. T. Kohlhepp, P. LeClair, L. Lagae, W. J. M. De Jonge, and B. Koopmans, *Phys. Rev. Lett.* **88**, 227201 (2002).
- [17] S. Anisimov, B. Kapeliovich, and T. Perelman, *Zh. Eksp. Teor. Fiz.* **66**, 375 (1974).
- [18] E. Beaurepaire, J.-C. Merle, A. Daunois, and J.-Y. Bigot, *Phys. Rev. Lett.* **76**, 4250 (1996).
- [19] J. GÜdde, U. Conrad, V. Jähnke, J. Hohlfeld, and E. Matthias, *Phys. Rev. B* **59**, R6608(R) (1999).
- [20] T. Saito, O. Matsuda, and O. B. Wright, *Phys. Rev. B* **67**, 205421 (2003).
- [21] S. Chikazumi and C. D. Graham, in *Physics of Ferromagnetism* (Oxford University Press, Oxford, England, 1997), p. 94.
- [22] M. Bombeck, A. S. Salasyuk, B. A. Glavin, A. V. Scherbakov, C. Brüggemann, D. R. Yakovlev, V. F. Sapega, X. Liu, J. K. Furdyna, A. V. Akimov, and M. Bayer, *Phys. Rev. B* **85**, 195324 (2012).
- [23] I. Razzolski, A. Alekhin, N. Ilin, J. P. Meyburg, V. Roddatis, D. Diesing, U. Bovensiepen, and A. Melnikov, *Nat. Commun.* **8**, 15007 (2017).
- [24] V. Besse, A. V. Golov, V. S. Vlasov, A. Alekhin, D. Kuzmin, I. V. Bychkov, L. N. Kotov, and V. V. Temnov, *J. Magn. Magn. Mater.* **502**, 166320 (2020).
- [25] C. Thomsen, H. T. Grahn, H. J. Maris, and J. Tauc, *Phys. Rev. B* **34**, 4129 (1986).
- [26] T. C. Zhu, H. J. Maris, and J. Tauc, *Phys. Rev. B* **44**, 4281 (1991).
- [27] Z. Lin, L. V. Zhigilei, and V. Celli, *Phys. Rev. B* **77**, 075133 (2008).
- [28] G. Traeger, L. Wenzel, and A. Hubert, *Phys. Status Solidi A* **131**, 201 (1992).
- [29] G. S. Krinchik and V. A. Artemjev, *J. Appl. Phys.* **39**, 1276 (1968).
- [30] R. Salikhov, A. Alekhin, T. Parpiiev, T. Pezeril, D. Makarov, R. Abrudan, R. Meckenstock, F. Radu, M. Farle, H. Zabel, and V. V. Temnov, *Phys. Rev. B* **99**, 104412 (2019).
- [31] A. Kimel, A. Zvezdin, S. Sharma, S. Shallcross, N. De Sousa, A. García-Martín, G. Salvan, J. Hamrle, O. Stejskal, J. McCord *et al.*, *J. Phys. D* **55**, 463003 (2022).